C. R. Physique 13 (2012) 837–852

Contents lists available at SciVerse ScienceDirect

Comptes Rendus Physique

www.sciencedirect.com

Nanophotonics and near field / Nanophotonique et champ proche

Raman spectroscopy and polarization: Selected case studies

Spectroscopie Raman et polarisation sur des cas d'étude choisis

Razvigor Ossikovski *, Gennaro Picardi, Gérald Ndong, Marc Chaigneau

LPICM, École polytechnique, CNRS, 91128 Palaiseau cedex, France

ARTICLE INFO

Article history:
Available online 28 July 2012

Keywords:
Raman spectroscopy
TERS
Polarization
Stress measurement

Mots-clés :
Spectroscopie Raman
Champ proche
Polarisation
Mesure de contraintes

ABSTRACT

We show, through several selected case studies, the potential benefits that can be obtained by controlling the polarization states of the exciting and scattered radiations in a Raman scattering experiment. When coupled with polarization control, Raman spectroscopy is thus capable of providing extra information on the structural properties of the materials under investigation. The experimental examples presented in this work are taken from the area of both conventional, i.e., far-field, as well as from near-field Raman spectroscopy. They cover topics such as the stress tensor measurement in strained semiconductor structures, the vibration mode assignment in pentacene thin films and the Raman scattering tensor determination from near-field measurements on azobenzene monolayers. The basic theory necessary for modelling the far- and near-field polarized Raman responses is also given and the model efficiency is illustrated on the experimental data.

© 2012 Académie des sciences. Published by Elsevier Masson SAS. All rights reserved.

RÉSUMÉ

A travers quelques cas d'étude choisis, nous mettons en évidence les bénéfices potentiels qui peuvent être tirés en contrôlant les états de polarisation des radiations excitatrice et diffusée dans une expérience de diffusion Raman. Couplée à un contrôle de la polarisation, la spectroscopie Raman est ainsi capable de fournir des informations supplémentaires sur les propriétés structurelles des matériaux étudiés. Les exemples d'expériences présentés dans ce travail proviennent à la fois du domaine de la spectroscopie Raman conventionnelle (c.-à-d., en champ lointain) et de celui de la spectroscopie en champ proche. Ils couvrent des sujets tels que la mesure du tenseur des efforts dans une structure semiconductrice contrainte, l'attribution des modes de vibration dans des couches minces de pentacène et la détermination du tenseur de diffusion Raman à partir de mesures en champ proche sur des monocouches d'azobenzène. La théorie de base nécessaire à la modélisation des réponses Raman polarisé en champs proche et lointain est également présentée et l'efficacité des modèles est illustrée sur les données expérimentales.

© 2012 Académie des sciences. Published by Elsevier Masson SAS. All rights reserved.

* Corresponding author.
E-mail address: razvigor.ossikovski@polytechnique.edu (R. Ossikovski).

1631-0705/$ – see front matter © 2012 Académie des sciences. Published by Elsevier Masson SAS. All rights reserved.
http://dx.doi.org/10.1016/j.crhy.2012.06.001

1. Introduction

Over the past forty years Raman spectroscopy has become a standard characterization technique in various areas of science and technology such as chemistry, geology, material science, biology, medicine, forensics and microelectronics, owing to its non-destructive nature, ease of use and absence of sample preparation [1–3]. As a simple "classic" example, Raman spectroscopy is capable, for the purposes of qualitative and quantitative chemical analysis, of supplying "fingerprint" spectra of any molecular species, providing in this way valuable information about its structure through an appropriate vibrational band assignment. Furthermore, the polarized nature of the Raman scattering phenomenon relates group theory, structure symmetry, Raman activity and scattering geometry to the measured Raman spectrum. Thus, the information obtained from a polarized Raman scattering experiment gives a deep insight into the molecular orientation or the crystal symmetry of the material under investigation. In particular, being extremely sensitive to modifications in the phonon spectrum induced by mechanical strain, polarized Raman spectroscopy has actually become one of the most efficient and widely used optical tools for stress measurements of a wide range of semiconductor structures and, in particular, silicon-based ones [3–6].

However, the spatial resolution of a standard Raman instrument equipped with a confocal microscope is restricted by the optical diffraction, resulting in the Rayleigh limit of the order of 1 μm (the exact value depending on the laser wavelength and objective used). Going beyond the diffraction limit requires a near-field optics approach resorting to techniques derived from Scanning near-field optical microscopy (SNOM). In the case of Raman spectroscopy, an effective increase in spatial resolution can be achieved by the technique of Tip-enhanced Raman scattering (TERS) whereby a metallic tip probing the sample surface plays the role of a nano-antenna. This near-field Raman spectroscopy "captures" the nanometer-scale spatial information which is lost in a conventional far-field experiment, thus allowing for Raman imaging with a spatial resolution down to several tens of nm [7–11].

The polarization-of-light aspect of Raman spectroscopy, whether performed in the far or in the near field is, however, quite often not fully exploited or even, simply overlooked. Besides the stress measurement application, in a typical Raman scattering experiment the polarization states of the exciting and scattered light are rarely controlled or, at best, the so-called depolarization ratio (ratio of the parallel-to-perpendicular, with respect to the scattering plane, scattered light intensities) is determined. Whereas the measurement of the depolarization ratio alone is sufficient for the characterization of isotropic (e.g., liquid or gaseous) samples [2], much more structural and chemical information can be in principle obtained on ordered (e.g., crystalline) materials through an appropriate polarization control during the experiment.

The main purpose of the present work is to reveal the important role played by the polarization of light in a Raman scattering experiment performed either in the far or in the near field and, more specifically, to illustrate, through several selected examples, the "added value" brought by the polarization control to the Raman characterization of materials. After a brief recall of the underlying theory and a description of the experimental setup, a review of four polarized Raman scattering case studies taken from both far-field and near-field (TERS) experiments is given and their respective implications are discussed. A conclusion and an outlook summarize the results and prospect future related experiments.

2. Theory

We shall restrict ourselves only to a brief recall of the master relations necessary for the quantitative description of a polarized Raman scattering experiment; a detailed first-principles presentation of the theory can be readily found in the literature [12].

The classical formalism of normal (i.e. non-resonant) vibrational Raman scattering is based on the well-known selection rule expressing the far-field scattered intensity I_{ff},

$$I_{ff} = K\left|\mathbf{e}_s^T \mathbf{R} \mathbf{e}_e\right|^2 \tag{1}$$

in which K is a proportionality constant, $\mathbf{e}_e$ and $\mathbf{e}_s$ are the exciting (or incident) and scattered electric field vectors respectively and $\mathbf{R}$ is the scattering tensor of the phonon vibration observed [1,2,13].

For cubic crystals such as Si and Ge there are three active orthogonal phonon modes described by their respective scattering tensors $\mathbf{R}_k$, $k = 1, 2, 3$, for the two transverse optical (TO_1 and TO_2) and one longitudinal optical (LO) phonon vibrations; in this case, the scattered intensity is given by the sum of the contributions of each mode [14],

$$I_{ff} = K\sum_k\left|\mathbf{e}_s^T \mathbf{R}_k \mathbf{e}_e\right|^2 \tag{2}$$

It should be noted that the matrix expression for the scattering tensor $\mathbf{R}$ entering Eq. (1) – as well as for $\mathbf{R}_k$ entering Eq. (2) – depends on the reference frame used. Usually, it takes its simplest form (with maximum number of zero components) if the crystallographic axes are used, as exemplified in the crystalline Si case (see Eqs. (11) in Section 4.1.1). In particular, if the sample is rotated about its normal, the tensor $\mathbf{R}$ will change accordingly; this change can be formally described by rotating the matrix of $\mathbf{R}$ with the help of a rotation matrix [15]. As a consequence, the scattered intensity given by Eq. (1) or (2) depends not only on the polarization states $\mathbf{e}_e$ and $\mathbf{e}_s$ of the exciting and scattered radiations, but also on the sample azimuth (or orientation) through the tensor $\mathbf{R}$ (or $\mathbf{R}_k$).

To describe the near-field scattering process, a phenomenological tip-amplification tensor $\mathbf{A}$ accounting for the preferential enhancement of the local electric field by the tip is introduced [15]. The tensor $\mathbf{A}$ expresses the fact that the electric

field component parallel to the tip axis is preferentially amplified compared to that perpendicular to it [16,17]. Its matrix representation in the tip-sample reference frame (x and y axes perpendicular to the tip axis, i.e. parallel to the sample plane; z axis along the tip axis) is

$$\mathbf{A} = \begin{pmatrix} b & 0 & 0 \\ 0 & b & 0 \\ 0 & 0 & a \end{pmatrix} \tag{3}$$

where a and b (with $a > b$) are phenomenological coefficients expressing the different amplifications of the electric field components parallel and perpendicular to the tip axis. The tip geometry (i.e., form, radius of curvature, apex angle) and material dielectric constant determine the actual values of the amplification factors.

The near-field (tip-enhanced) scattered intensity I_{nf} is given by

$$I_{nf} = K' \sum_k \left| \mathbf{e}_s^T \mathbf{R}'_k \mathbf{e}_e \right|^2 \tag{4}$$

where the near-field proportionality constant K' is generally different from K, the far-field one, and $\mathbf{R}'_k$ are the modified (or effective) Raman scattering tensors taking into account the action of the tip. Within the near-field scattering process, the polarization state of the exciting radiation is first modified by the tip, then phonon vibrations excited by this enhanced field generate the scattered radiation, and finally a second tip-scattered-radiation interaction takes place. As a result, the expression for the effective scattering tensors $\mathbf{R}'_k$ is

$$\mathbf{R}'_k = \mathbf{A}^T \mathbf{R}_k \mathbf{A} \tag{5}$$

in which $\mathbf{A}$ is the tip-amplification tensor from Eq. (3). Finally, the total scattered field intensity, I_{tf}, measured in "tip down" position, is given by the sum of the far-field, Eq. (1) or (2), and the near-field, Eq. (4), contributions,

$$I_{tf} = I_{ff} + I_{nf} \tag{6}$$

since the two signals superimpose incoherently on the detector. To account for the finite angle of the tip apex, usually the tensor $\mathbf{A}$, Eq. (3), is "tilted" from the tip axis at half the apex angle and the intensity contributions, obtained for evenly spaced azimuths about the tip axis, are averaged to produce the I_{nf} component entering Eq. (6) [15].

The above simple formalism is fully adequate to describe phenomenologically a near-field polarized light Raman scattering experiment.

3. Experimental

The core of the experimental setup used is a high-resolution (0.1 cm^{-1}) Raman spectrometer (Labram HR800 from HORIBA Jobin Yvon) in a confocal microscope backscattering configuration. The microscope is capable of accommodating objectives of various magnifications and numerical aperture (NA) values; the one used in the far-field studies was a 100× (NA = 0.9) objective from Olympus.

In order to perform oblique incidence (off axis) and near-field scattering experiments, the Raman spectrometer is optically coupled in oblique backscattering geometry to a scanning probe microscope or SPM (XE-100 from Park Systems). The long-working-distance objective (50×, NA = 0.45) is oriented at 55° with respect to the sample normal and produces an elliptical laser spot with approximate semi-axis lengths 2.5 μm × 1 μm at 633 nm laser wavelength. The opto-mechanical coupling is motorized along the x, y and z axes and allows for an accurate automated alignment of the exciting light spot with respect to the tip apex in near-field scattering (TERS) experiments. Fig. 1 shows the schematics of the experimental configuration.

Besides the excitation wavelength of 633 nm provided by the built-in HeNe laser of the spectrometer and typically used in the near-field studies, a tunable Ar laser (from Melles Griot; 458, 488 and 514 nm wavelengths used) can be employed in either the confocal or the oblique incidence configurations. The confocal configuration can be operated in the conventional (far-field) mode only.

In all TERS experiments, the SPM was operated in scanning tunnelling microscopy (STM) mode generally providing stronger enhancement and better reproducibility than the atomic force mode (AFM) [18]. The STM tips used were prepared from Au wire pieces of a 250-μm diameter and 99.99% purity (from Goodfellow) by electrochemical etching in a concentrated HCl/ethanol 1 : 1 solution according to an existing recipe [19].

In the polarized scattering experiments, the polarization states of the incident and scattered radiation can be continuously varied between 0° (p polarization; electric field parallel to the scattering plane) and 90° (s polarization; electric field perpendicular to the scattering plane) by using a half-wave plate and an analyzer respectively, inserted in motor-driven rotating mounts (0.1° uncertainty); see Fig. 1. In the oblique incidence (off axis) scattering configuration the scattering plane is defined by the direction of the incident/scattered radiation and the sample normal, coinciding with the tip axis (Fig. 1, left part). In the conventional confocal configuration (Fig. 1, right part), backscattering takes place along the sample normal and the scattering plane is undefined; p and s polarizations then refer to electric fields respectively parallel to the [100] and [010] crystallographic directions of a (001)-oriented c-Si sample (having its normal along the [001] direction).

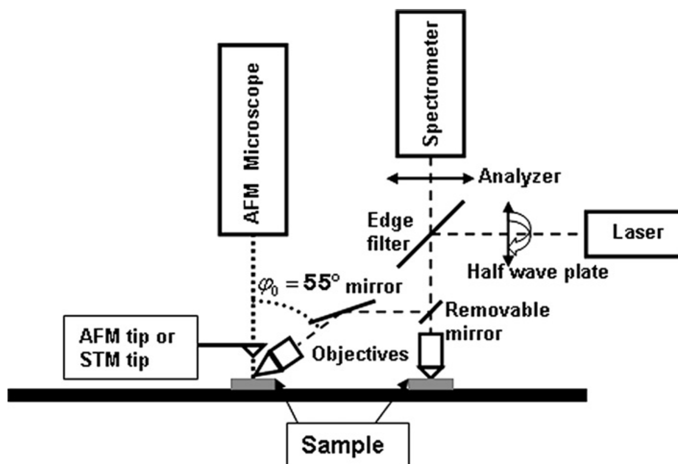

Fig. 1. Principle schematics of the experimental setup used in the polarized far-field and near-field Raman studies. The Raman spectrometer (on the right) is optically coupled in an oblique backscattering geometry to a scanning probe microscope (on the left). The spectrometer can be also operated (in the far field only) in conventional confocal Raman configuration. The polarization states of the incident and scattered radiation are controlled with a half-wave plate and an analyzer respectively.

4. Results and discussion

This section illustrates, on four selected case studies, the various opportunities and applications, actual or potential, opened up by polarized Raman spectroscopy and stemming from both far-field and near-field scattering experiments. The far-field topics cover the measurement of the stress tensor in strained semiconductor structures, of significant technological interest for the microelectronics industry, as well as the symmetry assignment of several vibration modes in pentacene thin films susceptible of being used in organic electronics devices. The near-field part of the section addresses the polarization aspects and the adequate modelling of the contrast enhancement in TERS experiments on crystals, together with the Raman scattering tensor determination of a vibration mode in an azobenzene self-assembled monolayer.

4.1. Far-field polarized Raman spectroscopy

Although the application of polarized spectroscopy techniques to solutes, organic and biological substances has been known to and used by chemists for many years [20,21], the opportunities offered by the polarization control of a Raman scattering experiment on crystals, patterned crystalline structures or other locally ordered materials (e.g., thin polymer layers) have not yet been fully addressed and exploited. Therefore, the aim of this subsection is to show the advantages that can be obtained (in terms of an increased amount of useful information) from the application of polarized Raman scattering to the stress characterization of Si-based microelectronic structures, as well as to the mode assignment of C–H chemical bond vibrations in pentacene thin films.

4.1.1. Stress measurements in strained semiconductor structures

Intentionally straining the channels of field-effect transistors in Si-based semiconductor structures during the fabrication process has become a standard method for increasing the carrier mobility and, consequently, the circuit performance in modern microelectronics industry [22]. The accurate measurement of strain, including highly resolved 2D mapping, is therefore a problem of significant technological interest and a number of strain characterization techniques such as grazing incidence X-ray diffraction, transmission electron microscopy and micro-Raman spectroscopy are currently employed to address it. Compared to the first two, the Raman spectroscopy based techniques are non-destructive, faster, easier to implement and do not require any sample preparation prior to measurement.

On the microscopic level, the strain induces changes in the equilibrium positions of the atoms in the semiconductor crystal. The phonon structure is consequently altered due to the anharmonic terms of the interatomic potential and, as a result, the phonon frequencies and Raman scattering tensors are modified. Monitoring the resulting changes in the mode frequencies represents a powerful method for strain measurement making Raman spectroscopy one of the techniques of choice for studying strain distributions in semiconductor devices [3–6].

Under the action of strain, the threefold degenerate optical phonon of a cubic crystal such as Si or Ge generally splits into three modes (TO_1, TO_2 and LO). The frequencies ω_i ($i = 1, 2, 3$) of the modes can be calculated within the quasi-harmonic approximation from the eigenvalues λ_i of the secular matrix [23]

$$\begin{pmatrix} p\varepsilon_{11} + q(\varepsilon_{22} + \varepsilon_{33}) & 2r\varepsilon_{12} & 2r\varepsilon_{13} \\ 2r\varepsilon_{21} & p\varepsilon_{22} + q(\varepsilon_{11} + \varepsilon_{33}) & 2r\varepsilon_{23} \\ 2r\varepsilon_{31} & 2r\varepsilon_{32} & p\varepsilon_{33} + q(\varepsilon_{11} + \varepsilon_{22}) \end{pmatrix} \tag{7}$$

by using the relation

$$\omega_i^2 = \omega_0^2 + \lambda_i \tag{8}$$

where ω_0 is the degenerate (unperturbed) phonon frequency ($\omega_0 \approx 521$ cm^{-1} for Si; $\omega_0 \approx 300$ cm^{-1} for Ge). In Eq. (7) the quantities p, q and r are the so-called phonon deformation potentials [5,24] ($p = -1.85\omega_0^2$, $q = -2.31\omega_0^2$ and $r = -0.71\omega_0^2$ for Si; $p = -1.45\omega_0^2$, $q = -1.95\omega_0^2$ and $r = -1.10\omega_0^2$ for Ge) and ε_{ij} are the components of the strain tensor $\boldsymbol{\varepsilon}$ related to the stress tensor $\boldsymbol{\sigma}$ through Hooke's law

$$\boldsymbol{\varepsilon} = \mathbf{S}\boldsymbol{\sigma} \tag{9}$$

in which the only non-zero components of the compliance tensor $\mathbf{S}$ for a cubic crystal (in contracted notation) are S_{11}, S_{12} and S_{44} ($S_{11} = 7.68 \times 10^{-6}$ (MPa)$^{-1}$, $S_{12} = -2.14 \times 10^{-6}$ (MPa)$^{-1}$ and $S_{44} = 12.7 \times 10^{-6}$ (MPa)$^{-1}$ for Si [5]; $S_{11} = 9.73 \times 10^{-6}$ (MPa)$^{-1}$, $S_{12} = -2.67 \times 10^{-6}$ (MPa)$^{-1}$ and $S_{44} = 14.9 \times 10^{-6}$ (MPa)$^{-1}$ for Ge). The modified Raman scattering tensors $\mathbf{R}'_i$ are obtained from the unperturbed ones, $\mathbf{R}_i$, from the relation [25]

$$\mathbf{R}'_i = v_{i1}\mathbf{R}_1 + v_{i2}\mathbf{R}_2 + v_{i3}\mathbf{R}_3 \tag{10}$$

in which v_{ij} is the j-th component of the eigenvector $\mathbf{v}_i$ (also called "phonon polarization vector") associated with the eigenvalue λ_i of the secular matrix, Eq. (7). The unperturbed scattering tensors $\mathbf{R}_i$ of the optical phonon modes TO$_1$, TO$_2$ and LO in a cubic crystal are respectively given by [13,14]

$$\mathbf{R}_1 = \begin{pmatrix} 0 & 0 & 0 \\ 0 & 0 & 1 \\ 0 & 1 & 0 \end{pmatrix}, \quad \mathbf{R}_2 = \begin{pmatrix} 0 & 0 & 1 \\ 0 & 0 & 0 \\ 1 & 0 & 0 \end{pmatrix} \quad \text{and} \quad \mathbf{R}_3 = \begin{pmatrix} 0 & 1 & 0 \\ 1 & 0 & 0 \\ 0 & 0 & 0 \end{pmatrix} \tag{11}$$

Eqs. (7) to (11), together with the appropriate selection rule, Eq. (2), are used to calculate the components of the stress tensor $\boldsymbol{\sigma}$ from the experimentally determined modified frequencies ω_i and intensities I_i of the Raman phonon lines.

It can be readily seen from the selection rule (2) and the expressions for the Raman tensors given by Eq. (11) that, in its conventional confocal (normal-incidence) backscattering on (001)-oriented cubic crystals, Raman spectroscopy is sensitive to the LO mode only [4,24]. However, to fully determine the stress tensor $\boldsymbol{\sigma}$ having six independent components in the general case, observations of all three optical modes are necessary. This can be achieved in practice by implementing either a large numerical aperture objective confocal [24,26,27] or an oblique (off-axis) [25,28] Raman backscattering configuration whereby all three modes are observable. When combined with an appropriate control of the incident (exciting) and scattered light polarization states, both scattering configurations are capable of measuring the full stress tensor in strained semiconductor structures [26,28].

For the stress levels encountered in current microelectronics structures (typically below ∼2000 MPa) the frequency splittings λ_i of the three optical modes are not large enough to make possible the observation of three distinct lines in the spectra. Instead, an unresolved "effective" peak resulting from the superposition of the three lines is observed. The frequency ω_{eff} and linewidth (full width at half maximum, FWHM) Γ_{eff} of the effective peak can be numerically calculated from the intensities I_i and frequencies ω_i of the three phonon modes, modified by the stress state $\boldsymbol{\sigma}$, as functions of the azimuth θ of the linear incident polarization state $\mathbf{e}_e$ set by the half-wave plate and entering the selection rule (2). The model thus obtained, corrected for the finite numerical aperture of the objective used [28], is fitted to the experimental values of $\omega_{eff}(\theta)$ and $\Gamma_{eff}(\theta)$ of the effective peak in the Raman spectra acquired at incident polarization azimuth values ranging from 0° to 180°. Monitoring experimentally the values of ω_{eff} and Γ_{eff} while scanning the azimuth θ of the incident polarization state $\mathbf{e}_e$ allows for an efficient over-determination of the unknown components of the stress tensor $\boldsymbol{\sigma}$ entering the model and makes possible a full tensorial analysis. In what follows, we consider a comparative example of the application of the above stress-determination methodology to strained microelectronics structures.

$Si_{1-x}Ge_x$ alloys with various Ge contents, or stoichiometries, x are widely employed at the process level for introducing strain in Si-based structures. Because of the lattice mismatch between the two materials, in a SiGe/Si (or a Si/SiGe) epitaxial structure, the strain induced in Si is tensile whereas the one in SiGe is compressive. The strain is strongest at the SiGe/Si interface and relaxes with distance on both sides. One of the simplest strained Si-based systems exploiting the lattice mismatch technique consists of a thin (typically, several tens of nm thick) strained SiGe (s-SiGe) layer epitaxially grown on a crystalline Si (c-Si) substrate. Fig. 2 shows the Raman spectrum, acquired at 458-nm laser wavelength, of a 100-nm-thick $Si_{1-x}Ge_x$ layer (with $x = 0.25$) grown on a (001)-oriented c-Si substrate. An intense peak at 520.5 cm^{-1} originating from the Si–Si optical phonon vibration in the unstrained Si substrate is accompanied by a slightly smaller one (usually appearing as a shoulder at low Ge contents or large probing light penetration depths) lying at a lower frequency (∼513 cm^{-1}) and corresponding to the same phonon in the s-SiGe layer. Most generally, the position of the Si–Si phonon vibration in a $Si_{1-x}Ge_x$ alloy depends both on its stoichiometry x and its strain state; for a strain-free alloy the peak frequency $\omega_{0\text{SiGe}}$ is given by the empirical relation [29]

$$\omega_{0\text{SiGe}} = 520.3 - 68x \tag{12}$$

In the presence of strain, this frequency is further shifted in accordance with Eq. (8).

In a simple homogeneous layer-on-substrate sample the stress state is at most biaxial, i.e. only two in-plane diagonal components, σ_{11} and σ_{22}, of the stress tensor $\boldsymbol{\sigma}$ have non-zero values. If σ_{11} and σ_{22} are taken to be oriented along the

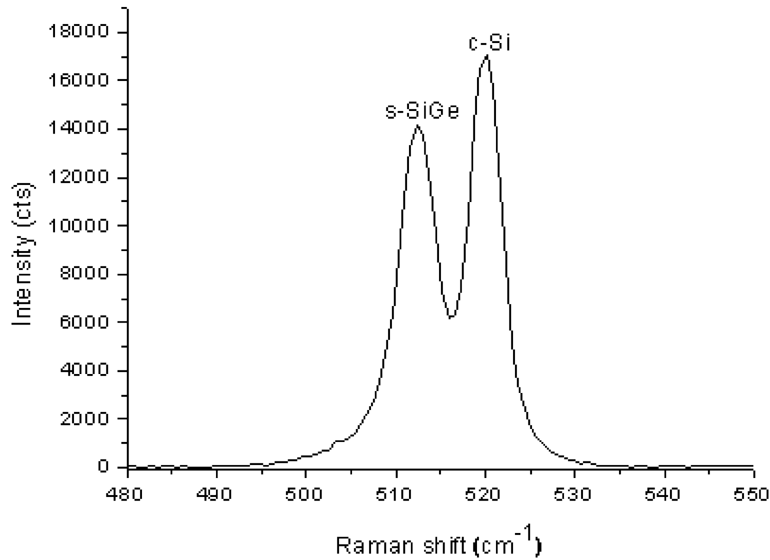

Fig. 2. Raman spectrum of a 100-nm-thick SiGe layer on a (001)-oriented *c*-Si substrate, obtained in the oblique backscattering configuration at 458-nm excitation wavelength. The Si–Si phonon vibrations of the unstrained Si substrate (stronger peak) and of the strained SiGe layer (weaker peak) are indicated.

[100] and [010] crystallographic directions respectively, then inserting Eq. (7) into (5) and solving the eigenvalue problem results into the following stress-induced frequency splittings of the optical phonon,

$$\lambda_{1,2} = \frac{1}{2}\left\{\left[p(S_{11}+S_{12}) + q(S_{11}+3S_{12})\right](\sigma_{11}+\sigma_{22}) \pm (p-q)(S_{11}-S_{12})(\sigma_{11}-\sigma_{22})\right\} \tag{13a}$$

$$\lambda_3 = \left[pS_{12} + q(S_{11}+S_{12})\right](\sigma_{11}+\sigma_{22}) \tag{13b}$$

(In Eqs. (13), the compliance tensor components S_{ij} as well as the phonon deformation potentials p and q are obtained as linear combinations of the values for Si and Ge taken with their respective weights, $1-x$ and x; the "unstrained" frequency entering the phonon deformation potentials is the one given by Eq. (12).)

As mentioned earlier, the only observable LO phonon splitting λ_3 in the conventional low numerical aperture objective confocal backscattering configuration depends on the sum $\sigma_{11}+\sigma_{22}$ of the two non-zero stress tensor components ($\sigma_{11}+\sigma_{22}$, the trace of the $\boldsymbol{\sigma}$ tensor, is the so-called hydrostatic stress component) and the independent determination of σ_{11} and σ_{22} is impossible in this case. In order to retrieve σ_{11} and σ_{22} (and thus, completely determine the biaxial stress tensor $\boldsymbol{\sigma}$) experimental observations of the TO_1 and TO_2 splittings λ_1 and λ_2 are necessary. Note that the Raman scattering tensors given by Eq. (11) are not modified by the stress since the latter is directed along the crystallographic axes [100] and [010] that are also eigenaxes of the secular matrix (7).

Figs. 3(a) and 3(b) represent respectively the peak frequency ω_{eff} and FWHM Γ_{eff} of the "effective" Si–Si phonon line, resulting from the contributions of the three phonon modes, of the *s*-SiGe layer as functions of the incident polarization azimuth, after Lorentzian lineshape deconvolution. The solid lines are the fitted curves, according to the theory from Ref. [28], of the frequency and FWHM to the stress state $\sigma_{11} = \sigma_{22} = -2040$ MPa in the *s*-SiGe layer. For comparison, the frequency and FWHM of the *c*-Si substrate peak, together with their respective "unstrained" values, 520.5 cm^{-1} and 3.0 cm^{-1}, are also shown; as expected, they are independent of the incident polarization state: since the *c*-Si substrate is much thicker than the 100-nm-thin *s*-SiGe layer, it can be consequently considered as virtually relaxed within the ∼0.55-μm penetration depth of the 458-nm Ar laser line in Si. The *s*-SiGe layer being isotropic (i.e., not exhibiting any patterns or other structural macroscopic anisotropy), its stress state is bisotropic, i.e. $\sigma_{11} = \sigma_{22}$, as determined from the fits. In particular, a closer look on the data shows that the fitted ω_{eff} and Γ_{eff} curves are both symmetric about the 90°-azimuth value; this is a direct result of the unique splitting $\lambda_1 = \lambda_2$ for both TO modes. (As readily seen from Eq. (13a), $\sigma_{11} = \sigma_{22}$ implies $\lambda_1 = \lambda_2$ and vice versa.) The ω_{eff} fits further yield the stress value, together with its negative sign accounting for a compressive stress state. Unlike the ω_{eff} fitted curves, the Γ_{eff} curves agree only qualitatively with the data, the latter exhibiting too much scatter for polarization azimuths around 90°, possibly due to different broadening of the TO and LO phonon modes in $Si_{1-x}Ge_x$ alloys at large x values unaccounted for in our model; nevertheless, the FWHM values for SiGe alloy layer are larger than those of the (unalloyed) *c*-Si substrate and further increase at close to 90° azimuths, as expected. It should be also noted that, unlike the peak frequency and linewidth, the intensity of the *s*-SiGe layer phonon effective peak (not shown) is practically insensitive to the stress state since depending essentially on the incident polarization state in accordance with the "squared cosine" behaviour following from the selection rule (2); besides exhibiting a larger amplitude, the intensity curve of the unstrained *c*-Si substrate has identical qualitative behaviour.

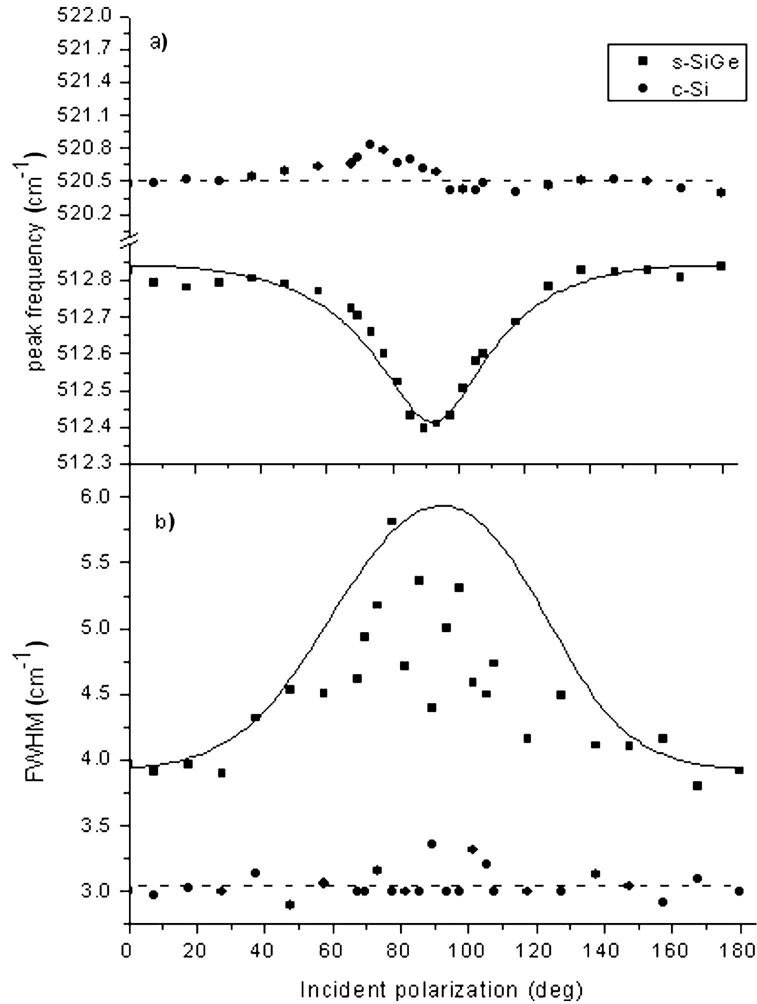

Fig. 3. Measured (dots) and fitted (lines) peak frequency (a) and FWMH (b) for the strained SiGe-lattice vibration and for the unstrained Si substrate as functions of the incident polarization obtained in the oblique (off-axis) Raman backscattering configuration.

The *s*-SiGe/*c*-Si structure was further measured in conventional confocal scattering configuration using a large numerical aperture (NA = 0.9) objective. Figs. 4(a) and 4(b) show respectively the frequencies and FWHM of the Si phonon peak originating from the *s*-SiGe layer and *c*-Si substrate, together with the fitted curves according to the theory from Ref. [26]. The experimental data and fits look qualitatively the same as those from Figs. 3(a) and 3(b); the stress tensor component values derived from both scattering configurations, oblique and confocal, coincide. This is readily understandable since both configurations are capable of exciting all three Si optical phonon modes, as previously mentioned: the oblique incidence one takes advantage of the skew angle (55° in our setup) between the probing (as well as scattered) light direction and the [001] crystallographic direction (i.e. the sample normal of a (001)-oriented crystal) whereas the confocal configuration exploits the skew marginal rays of the scattered radiation collected by the large numerical aperture objective. The purpose of varying the polarization state of the incident probing light in both configurations is identical: as directly follows from the selection rule (2), for azimuth values close to 0° (and 180°) it is the LO mode that is preferentially excited whereas for azimuths around 90° the contributions of the two TO modes are most important, with the LO mode response attaining a minimum. All three mode contributions add to form an effective phonon peak whose frequency and linewidth are both polarization and stress dependent: in particular, symmetric peak frequencies and FWHMs indicate a bisotropic plane stress state, as discussed; compare Figs. 3 and 4. Note that, although producing similar results, both configurations differ not only in scattering geometry but also in objective numerical apertures: while the confocal one uses a large numerical aperture objective as already mentioned (NA = 0.9), the oblique incidence one features an NA value of 0.45 only. Clearly, the low numerical aperture in the latter case is “compensated“ by the large incidence angle (55°; see Fig. 1, left) while, conversely, the large numerical aperture in the confocal case “compensates” for the “inconvenient” [001] crystallographic normal backscattering direction.

In summary, the SiGe/Si-case study clearly demonstrates the practical applicability of the stress-determination methodology, experimentally based on the polarized oblique or large numerical aperture confocal backscattering Raman spectroscopy

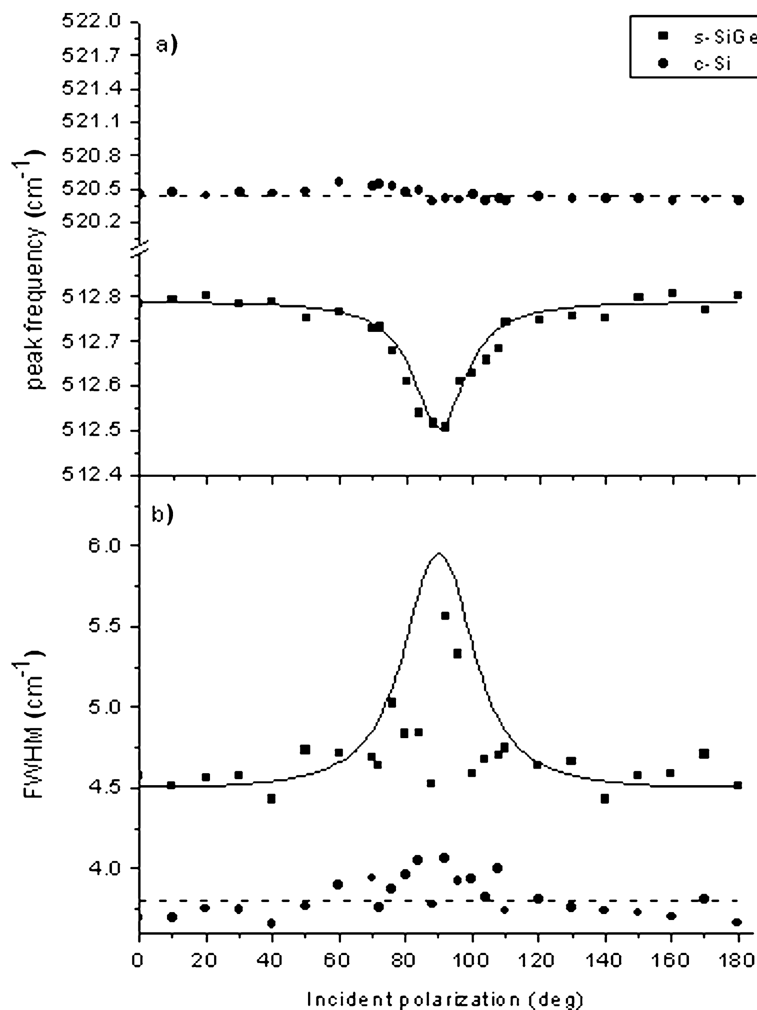

Fig. 4. Measured (dots) and fitted (lines) peak frequency (a) and FWMH (b) for the strained SiGe-lattice vibration and for the unstrained Si substrate as functions of the incident polarization obtained in the confocal (normal incidence) Raman backscattering configuration.

configurations. Full stress tensor determination, signs included, can be achieved by varying the polarization state of the incident laser radiation. The accuracy of the methodology can be estimated to be of the order of several tens of MPa, the exact value depending on the stress tensor form (diagonal or not) and nature (hydrostatic, uniaxial, bisotropic, biaxial), as well as on the Raman intensity signal-to-noise ratio, instrument spectral resolution and the efficient numerical deconvolution of the spectral lines.

4.1.2. Raman vibration mode identification in pentacene thin films

Pentacene ($C_{22}H_{14}$) has recently become a subject of active research owing to its p-type-semiconductor-like behaviour with mobility values reaching those of amorphous silicon, thus making it a good candidate for organic electronics applications [30]. Understanding the structural properties of pentacene layers at the molecular level is of crucial importance for the improvement of their transport properties and, consequently, for the increase in efficiency of the pentacene-based electro-organic devices. Polarized Raman spectroscopy is particularly well suited for such characterization studies since it gives access to the molecular vibrations that directly depend on the molecular organization and the material microstructure. In particular, the use of polarized light allows for an unambiguous assignment of the vibration mode symmetries.

The sample under investigation was a 12-nm-thin layer of pentacene thermally evaporated on a (100)-oriented Si wafer under high vacuum conditions (5×10^{-7} mbar) at the deposition rate of 1 nm/s. The wafer was cleaned following the conventional microelectronics steps [31].

In this polarized Raman study, we focused on the spectral range 1140–1200 cm^{-1} corresponding to the in-plane C–H bond bending vibrations. The two major features occurring in this frequency range comprise several finer peaks whose origin and assignment are controversial at present [32–34]. The large number of vibration-involved atoms makes it difficult for theoretical calculations to predict the position, intensity and symmetry of the Raman active modes. However, the polarization

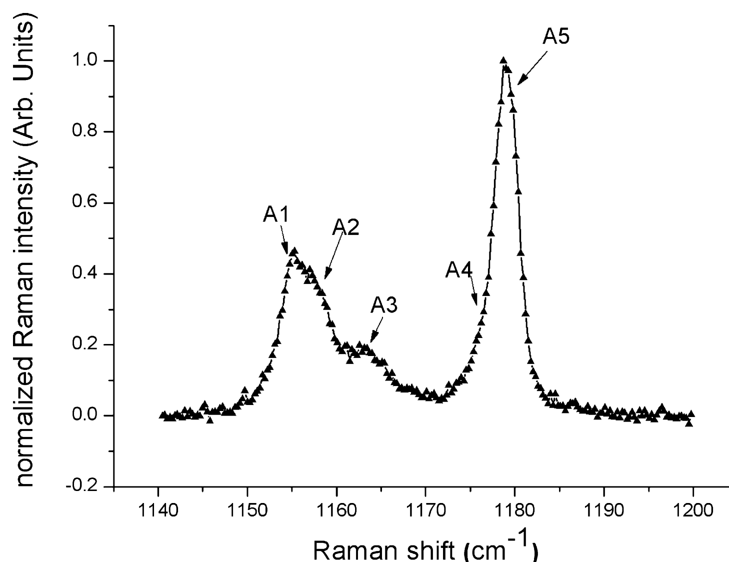

Fig. 5. Raman spectrum of a thin pentacene layer acquired in conventional confocal configuration (at a 633-nm excitation) for 45° incident polarization (with respect to the analyzer). The five resolved lines (A_i, $i = 1$ to 5) of the C–H bond bending vibrations are indicated.

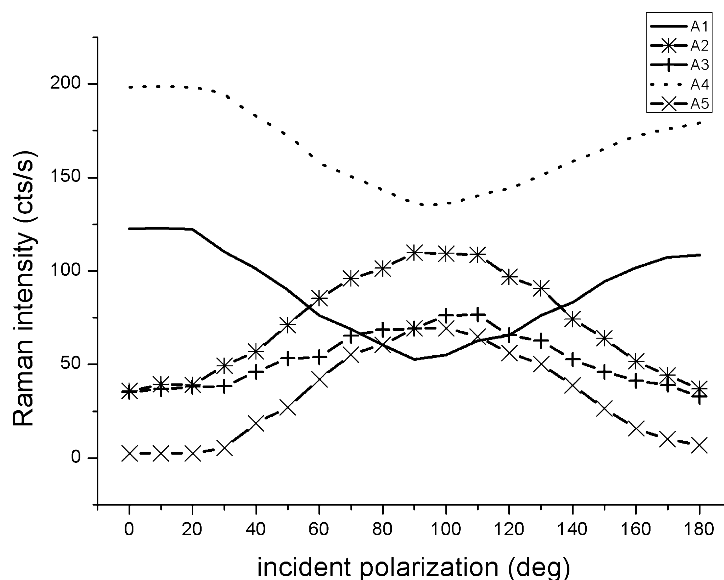

Fig. 6. Peak intensities of the five Raman lines of pentacene in the 1140–1200 cm^{-1} spectral range as functions of the incident polarization.

properties of Raman scattering expressed in the selection rule (1), combined with group symmetry considerations, can be used to clearly identify and distinguish uncoupled (intermolecular) from coupled (intramolecular) vibration modes.

Fig. 5 presents the polarized confocal backscattering Raman spectra (633-nm wavelength excitation) of the pentacene layer in the frequency range of interest. The spectrum was recorded for an incident (exciting) polarization state making a 45° azimuth with the scattered light polarization state. Qualitatively similar Raman bands, showing two main features at 1158 cm^{-1} and 1178 cm^{-1}, were observed whatever the incident polarization state. The first band was decomposed into a sum of three Lorentzian lines, denoted by A1, A2 and A3, by using a fitting procedure providing the intensity, position and FWMH of each individual line; the second feature was similarly decomposed into two more Lorentzian peaks, A4 and A5, in accordance with the literature [35].

In the polarized experiment, the azimuth of the incident polarization state was varied from 0° to 180° (through steps of 10°) by rotating the half-wave plate while the analyzer, setting the polarization state of the scattered radiation, was kept fixed and its transmission axis served as a zero reference for the above azimuth values. Fig. 6 shows the integrated intensity of the A*i* peak ($i = 1$ to 5) as a function of the incident polarization azimuth. All five peak intensities exhibit the squared-sine-like behaviour in accordance with selection rule (1); however, A1- and A4-peak intensities attain their minimum values

for a 90° incident polarization, whereas peaks A2, A3 and A5 exhibit an opposite behaviour with minima reached for 0° (and 180°) polarization azimuth.

This qualitative difference in mode behaviour can be understood by employing symmetry considerations and numerical simulations as follows. Since the Raman-active modes of a single (i.e., isolated) molecule have the same symmetry as the molecule itself and the symmetry group of pentacene is D_{2h}, then the uncoupled (i.e., intramolecular) Raman modes may be only of A_g, B_{1g}, B_{2g} or B_{3g} symmetry [12,36]. For in-plane C–H bending modes we are concerned with, the symmetry group is A_g with the corresponding Raman scattering tensor being given by

$$\mathbf{R}_{Ag} = \begin{pmatrix} \alpha_{xx} & 0 & 0 \\ 0 & \alpha_{yy} & 0 \\ 0 & 0 & \alpha_{zz} \end{pmatrix} \tag{14}$$

where $\alpha_{xx} = 91$, $\alpha_{yy} = 37$ and $\alpha_{zz} = 17$ [37]. (The tensor is expressed in the molecule reference frame; the x and y axes are lying on the molecular plane along the longer and shorter molecule dimension, respectively; the z axis is oriented along the plane normal.)

When thermally evaporated in a thin (several tens of nm thick) layer, pentacene forms ~200-nm-large islands composed of several molecular layers each [31]. Within a single island, the individual molecules are preferentially oriented so that their longer dimension axes make a 10°-tilt with respect to the layer normal [38]. Further, the Raman laser spot (~1-μm diameter) illuminates a large number of pentacene islands that can be considered to be randomly oriented and consequently, the scattered light intensity will be that of a single molecule with the tensor $\mathbf{R}_{Ag}$ (14) whose response is averaged over all possible rotation angles of its 10°-tilted longer axis about the layer normal. The corresponding numerical simulation of the detected intensity exhibits a minimum for a 90° incident polarization and a maximum for 0° (and 180°) one. Such polarization behaviour is in full agreement with that of the A1 and A4 peak intensities and opposite to that of A2, A3 and A5 peaks; see Fig. 6. Consequently, it can be inferred that A1 and A4 modes possess the A_g symmetry of the D_{2h} point group and therefore can be unambiguously attributed to the uncoupled (intramolecular) vibrations of the pentacene molecule. In particular, A1 can be assigned to the C–H in-plane bending vibrations of atoms at the two molecule ends, whereas A4 originates from atoms located along the sides of the molecule, in confirmation of the tentative assignment from the literature [33,34]. The other three remaining lines, A2, A3 and A5, come most probably from coupled modes involving several neighbouring molecules. The exact symmetry of these contributions is harder to determine since a certain number of symmetry groups different from that of an isolated molecule should enter into consideration. Thus, using the difference in the polarization dependence of the Raman responses of the modes, it is possible to discriminate between the different symmetries and arrive at mode assignment. A more detailed account of this study can be found in Ref. [31].

4.2. Near-field polarized Raman spectroscopy

As mentioned in the Introduction, in the basis of the TERS effect lies the strong local enhancement of the electromagnetic field occurring at the apex of a sharp noble-metal tip when illuminated with a tightly focused laser light. The phenomenon results from the combination of an electromagnetic 'lightning rod effect' and a localized surface plasmon (LSP) excitation. The antenna-like tip acts as a scattering centre partially converting the incoming far-field radiation into an enhanced near field, in a region with dimensions determined by the size of the tip apex (typically less than 50 nm). The Raman scattering process takes directly advantage from this enhancement since the scattering cross-section scales with the fourth power of the (local) electromagnetic field enhancement. TERS is extremely efficient in detecting molecules adsorbed on flat metal surfaces, down to single-molecule sensitivity [39,10]. By combining point-by-point tip scanning with simultaneous spectrum acquisition, near-field Raman mappings can be performed with lateral resolutions down to tens of nm [40,41,11].

In a TERS experiment, the metal tip not only enhances the local field, but also modifies the polarization state of both the exciting and scattered radiations as described by the phenomenological model presented in Section 2. One of the purposes of this subsection is to show the quantitative validity of the phenomenological approach when applied to near-field Raman scattering on a crystalline Si (c-Si) substrate. In a second study, the polarization approach is used to derive the Raman scattering tensor of self-assembled organic molecules (an azobenzene monolayer) from their TERS polarization properties, thus extending the validity of the model to the case of ordered non-crystalline materials.

4.2.1. Polarized near-field Raman spectroscopy on a c-Si sample

The model presented in Section 2 quantitatively describes the changes in the polarization states induced by the tip to both the exciting and scattered radiations and allows for the complete simulation of the TERS experiments on crystalline (c-Si) samples. Eq. (2) gives the far-field contribution (corresponding to the experiment with the tip retracted) whereas Eqs. (3) to (5) provide the near-field response component. Finally, the total field scattered intensity (corresponding to the experiment with the tip tunnelling) is calculated from Eq. (6). The Raman scattering tensors of the Si–Si optical phonon given by Eq. (11) are used in calculating both field components.

In the experiment, the incident angle and polarization state of the exciting radiation, the polarization state of the detected scattered radiation and the azimuth orientation of the crystalline sample (on which the expressions of the Raman scattering tensor depend) are fixed parameters that enter the simulation procedure. Knowing the values of these parameters, the far-field Raman scattered radiation can be readily obtained as a function of the polarization state of the incident

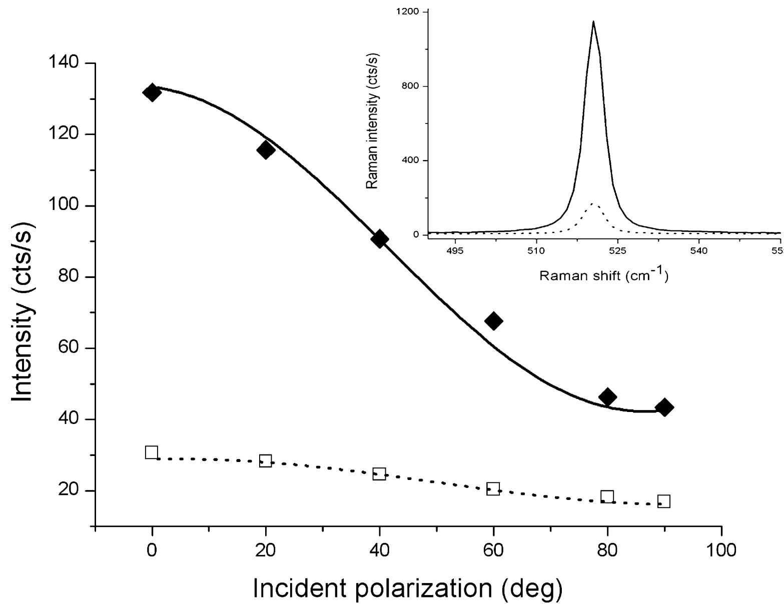

Fig. 7. Intensities of the Si–Si phonon band of (111)-oriented *c*-Si as functions of the incident polarization, obtained in the tip-in-tunnelling mode (diamonds; fit in solid line) and the tip-retracted mode (squares; fit in dotted line). Inset: tip-tunnelling (solid line) and tip-retracted (dotted line) Raman spectra of the Si–Si phonon band (633-nm excitation wavelength).

light. The calculated curve has to be further re-scaled, through fitting, to reproduce the actual data; this step amounts to the determination of the “calibration” factor K entering Eqs. (1) and (2).

To properly weight the near-field contribution to the total scattered intensity (measured with the tip in tunnelling mode), it is likewise necessary to know the “near-field” proportionality constant K' entering Eq. (4). Physically, the K'-to-K ratio is given by the proportion of the number of scatterers excited by the tip-enhanced field to those contributing to the far-field only. However, the near-field response further depends on the “tip amplification” factors a and b entering the tensor $\mathbf{A}$ given by Eq. (3). The latter depend strongly on the tip form, material and structure and cannot be easily estimated [16]. As a consequence, one usually “incorporates” the b coefficient into the factor K' (i.e., takes the product bK' as a fitting parameter) and considers only the a-to-b ratio instead of considering a and b separately. By doing so, one focuses only on the polarization properties of the TERS experiment disregarding the absolute values of the enhancements.

The samples used to test the validity of the near-field modelling theory were pieces of n-doped (111)-oriented c-Si wafers (from ITME, Poland; 0.05–0.01 Ω·cm resistivity). Oxide-free sample surface appropriate for tunnelling was achieved by performing two cycles of oxidation in a 3 : 1 concentrated H_2SO_4/30% H_2O_2 and a subsequent etching in 40% NH_4F. The Raman scattering setup was operated in oblique incidence geometry at 633-nm excitation wavelength and in the STM-TERS mode. The tip bias voltage was −1.0 V relative to the sample resulting in a 0.1-nA tunnelling current.

The spectra of the optical phonon Si–Si Raman band acquired, respectively, with the tip in tunnelling (total-field spectrum, upper solid line) and in withdrawn position (far-field spectrum, lower dotted line), are shown in the inset of Fig. 7 for a p-polarized exciting light. (Recall that p-polarized light is the one whose electric field is parallel to the scattering plane.) The Raman peak intensity is clearly higher with the tip tunnelling than with the tip retracted.

The corresponding total-field (tip tunnelling) and far-field (tip retracted) scattered light intensities are also represented in the figure as functions of the exciting light polarization azimuth (varied from p to s polarization by steps of 20°). The analyzer azimuth was set at 90° (s polarization). As expected, the highest intensity is achieved for p polarization (0° azimuth) and the lowest one, for s polarization (90° azimuth). By using the simulation procedure described above, the total-field intensity data were very well fitted to the model (the solid curve in Fig. 7) yielding an a-to-b ratio equal to 1.6 : 1. Such a value of the a-to-b ratio is characteristic of a weakly to moderately polarization sensitive tip (recall that the corresponding enhancement factors scale as the fourth power of a and b [16]).

The far-field intensity experimental data (squares) and corresponding fit (dotted line curve) represented in the lower part of Fig. 7 are less polarization dependent than the total-field ones. Consequently, the near-to-far-field contrast (given by the ratio of the two curves minus one) is relatively important. It should be noted that, in the oblique incidence backscattering geometry, the orientation (azimuth) of the crystalline sample about its normal transforms the Raman scattering tensors $\mathbf{R}_k$ from Eq. (11) and consequently, modifies the relative probabilities of excitation of the three degenerate optical phonon modes. The polarization state of the scattered radiation thus changes with the sample orientation and this fact influences both the far-field and near-field scattered intensities, especially when an analyzer is present in the output beam. In this experiment, the sample was rotated about its normal so as its $[1\bar{1}0]$ crystallographic axis made a 70° azimuth with the scattering plane in order to maximize the near-to-far-field contrast value. A high contrast value, as the one shown in Fig. 7,

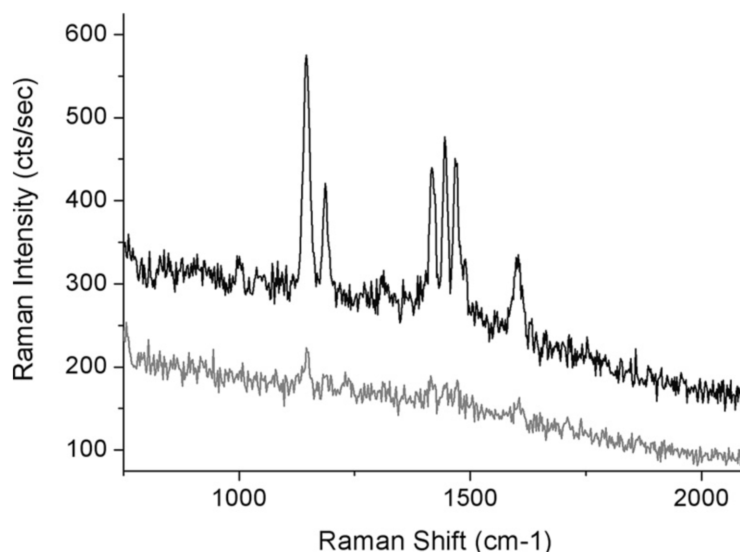

Fig. 8. Raman spectra of an azobenzene monolayer grafted on an Au(111) substrate, obtained in oblique backscattering configuration (633 nm). Lower trace: tip-retracted mode; upper trace: tip-in-tunnelling mode.

can thus be achieved even for a moderately enhancing tip through an appropriate choice of the sample orientation azimuth, the incident polarization state and the analyzer setting [42].

The above considerations can be used in practice in the so-called "contrast enhancement method" [43]. Physically, in the near-field ("tip tunnelling") mode both the exciting and scattered radiations are partially "depolarized" by the tip preferentially enhancing the electric field component parallel to its axis, whereas in the far-field ("tip retracted") mode the polarization state of the scattered radiation is determined by the Raman scattering tensor of the phonon mode and the polarization of the exciting radiation; see Eqs. (1) and (2). As a result, the near-field and far-field components of the scattered light generally exhibit different polarization behaviours. This "polarization dependence effect" can be used for the suppression of the far-field component in the total signal. Indeed, the far-field contribution can be strongly attenuated with the introduction of an analyzer in the scattered beam. As a consequence, the effective value of the contrast defined as the ratio of the total field ("tip tunnelling") scattered light intensity to the far-field ("tip retracted") one increases; the values thus obtained reach 4.4 for the *p*-polarized incident light and 2.6 for the *s*-polarized one.

Eventually, it should be stressed that the tip polarization model is a phenomenological one, i.e. it may equally well account for near-field scattering phenomena, as well as for macroscopic artefacts influencing the polarization state (e.g., a "mirror effect" by the tip). Whereas scattering artefacts are highly unlikely in STM-TERS whereby there is a tunnelling gap between the wire-made sharp tip and the sample, they might be partially present in an AFM-TERS experiment involving a relatively large pyramidal or conical tip fixed below a relatively large shaft [44]. A polarization behaviour in accordance with the model is not a guarantee for a near-field experiment; to ascertain the presence of a near-field contribution to the scattered signal (as well as to quantify it with respect to the far-field one) either a scanning (or mapping) experiment showing sub-wavelength spatial resolution [11] or a tip approach curve recording [44,45] should be performed.

4.2.2. Near-field characterization of azobenzene monolayers

Thiol self-assembled monolayers (SAMs) deposited on a gold surface form domain-like structures possessing a high degree of order with virtually all the molecules being identically oriented with respect to the surface plane [46]. This makes SAMs particularly interesting for polarized TERS studies in order to further test the phenomenological polarization model from Section 2 on ordered non-crystalline structures. Furthermore, azobenzene thiol is of special scientific and technological interest because of its reversible photo-activity property potentially suitable for a whole range of applications such as molecular electronics, chemical sensing and photo-patterning.

The synthesis of the azobenzene thiol used in the TERS experiments closely followed the recipe reported in Ref. [47]. The molecules were grafted on a freshly flame-annealed Au(111) substrate (from Arrandee). The tunnelling parameters employed in the STM-TERS measurements were 0.05–1.5 V for the bias voltage (positive tip), and 30–40 pA for the tunnelling current [45].

A typical example of a TERS experiment on an azobenzene monolayer is presented in Fig. 8. The spectra were recorded for incident *p* polarization with a 1-s integration time and a laser power of 0.5 mW to minimize any photo-degradation of the organic layer. The lower trace refers to the far-field signal when the tip is retracted few microns above the sample surface; the upper trace is relative to the tip-in-tunnelling mode. The near-field-to-far-field contrast ratio derived from the two spectra was ten [45] which corresponds to a TERS enhancement factor of at least 10^4. Assignment of the Raman active modes is readily available in the literature [48,49]. Six major spectral features attributable to the vibrations of the anchored

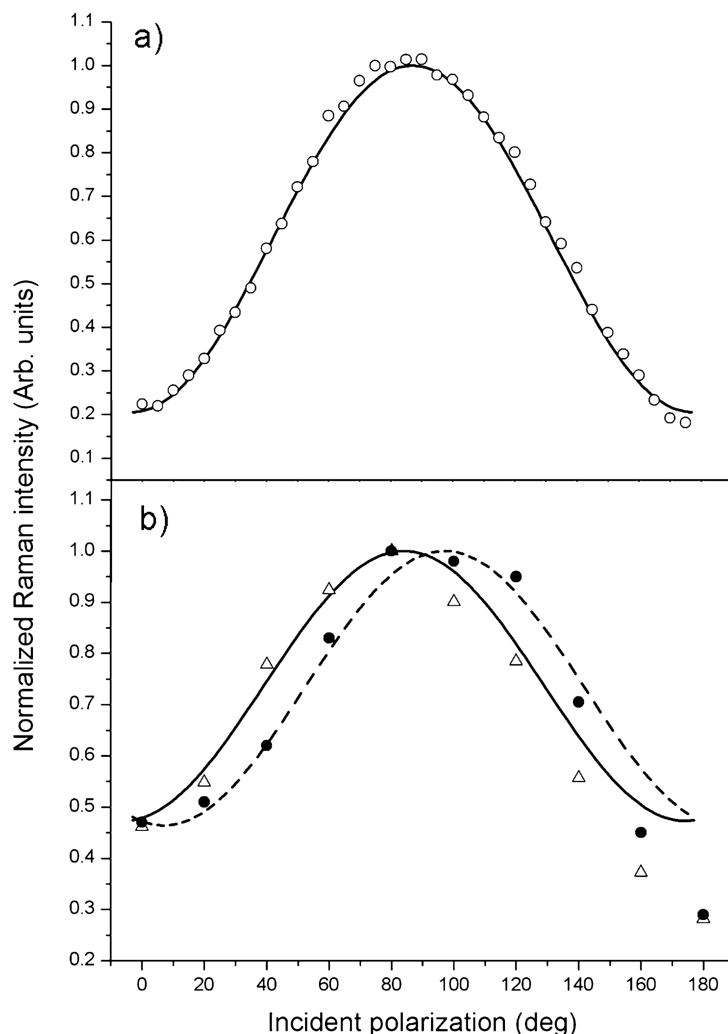

Fig. 9. Normalized peak intensity of the azobenzene ν_{15} Raman mode as a function of the incident light polarization, (a) in the far field (tip retracted), and (b) in the near field (tip tunnelling) at two different tip positions over the sample. The lines show the best fits to the data.

double-ring system are clearly seen in the TERS spectrum (whereas the far-field one is almost featureless). More specifically, all observed bands in Fig. 8 correspond to in-plane vibrations with A_g symmetry and mostly couple with the normal-to-the-surface local electric field component, due to the perpendicular orientation of the azobenzene moieties [50,51]. In the following, we focus on the strongest peak at 1141 cm^{-1} assigned to the in-phase stretching of the two C–N bonds (ν_{15}).

The effect of the exciting light polarization state (at 633 nm) on the scattered Raman intensity from the azobenzene thiol layer is reported in Fig. 9. There was no analyzer in the output beam (the so-called “depolarized” or, more correctly, unanalyzed scattering configuration). The far-field spectrum in Fig. 9(a) was acquired at higher laser power (5 mW) and longer accumulation time (20 s). In the absence of the tip, surface selection rule applied to the response of the planar molecule chemisorbed at the metal surface further confirms that, over the large illuminated area, most of the azobenzene domains have their molecule longer axes oriented parallel to the sample normal.

Two sets of data for the near-field integrated intensity of the ν_{15}-mode peak versus the incident polarization azimuth, corresponding to two different tunnelling positions on the sample surface, are reported in Fig. 9(b). The azimuth values were swept from 0° to 180° by steps of 20°. Note that, in this study, unlike in the preceding ones, the origin of the azimuths corresponds to *s* polarization that is, 0° stand for an exciting electric field perpendicular to the scattering plane. This allows for a better readability of Fig. 9 curves since, with this choice, they all attain their maxima roughly in the middle of the *x* axis range. Indeed, maximum tip enhancement is achieved for *p*-polarized incident light having its electric field parallel to the scattering plane (and therefore, maximizing the component along the tip axis), as expected.

The azobenzene molecule in the *trans* conformation belongs to the C_{2h} spatial point group [48,49] which results in a Raman scattering tensor with four independent components for A_g-symmetry active modes. Taking the *z* axis along the

surface normal and identifying the *xz* plane as the molecular plane, the Raman tensor $\mathbf{R}_{Ag}$ of a single azobenzene molecule has the general form

$$\mathbf{R}_{Ag} = \begin{pmatrix} \alpha_{xx} & 0 & \alpha_{xz} \\ 0 & \alpha_{yy} & 0 \\ \alpha_{xz} & 0 & \alpha_{zz} \end{pmatrix} \tag{15}$$

As reported by Pedersen et al. [52] for the azobenzene chromophore in the *trans* configuration, both the absorption cross-section along the y axis and the polarizability tensor component normal to the molecular plane, i.e., the yy component, are negligible at the exciting wavelength used in our experiments (note the different labeling of the molecular axes used here with respect to that of the cited reference). Keeping in mind that the Raman tensor is the spatial derivative of the polarizability tensor with respect to the normal mode vibrations (here, the ν_{15} mode), we assume the yy polarizability component to change only weakly with the ν_{15} molecular vibration analyzed here, allowing to simplify the above tensor form by setting $\alpha_{yy} = 0$ in Eq. (15). Further, the Raman tensor for the monolayer may be obtained from a superposition of the Raman tensors of the single molecules within the unit cell of the type of lattice formed. As previously mentioned, high-resolution topographic investigations on azobenzene thiol SAMs evidence the existence of small regular domains (∼20 nm diameter) surrounded by disordered zones [47,53,54]. These domains are reported as having an (oblique) nearly rectangular lattice with two molecules per unit cell. The two molecules may be almost parallel or form an angle. For a parallel dimer the molecular lattice tensor retains the single-molecule form (15). In the second case of two molecules forming an angle of approximately 40° between their short molecular axes (the longer axis being along the z axis) [47], the resulting unit cell tensor is obtained by summing the individual tensors of the two molecules, the second tensor being rotated at the angle of 40° with respect to the first one:

$$\mathbf{R}_{azo} = \mathbf{R}_{Ag} + \mathbf{T}^{T}(40^\circ)\mathbf{R}_{Ag}\mathbf{T}(40^\circ) \tag{16}$$

In Eq. (7), the transformation matrix $\mathbf{T}$ is simply a rotation matrix about the z axis at the angle $\theta = 40^\circ$ [55].

The region probed below the tip in the TERS experiments has a size comparable to that of the small ordered domains; we can thus speculate that the near-field polarization dependent response will be different from its far-field counterpart whereby a much larger area encompassing a large number of differently oriented domains together with, possibly, disordered zones are probed. The above tensor $\mathbf{R}_{azo}$ is used in the TERS simulation procedure described in the preceding subsection to fit the "tip tunnelling" response of the azobenzene layer shown in Fig. 9(b) (the element α_{zz} was set equal to unity because of the relative nature of the polarized TERS model; see the discussion from the previous subsection). Note that the tensor $\mathbf{R}_{azo}$ from Eq. (16) corresponds to the *xz* plane coinciding with the scattering plane; to account for the various possible orientations of the domain lattice with respect to the scattering plane, $\mathbf{R}_{azo}$ should be further rotated about the z axis (i.e., the sample normal) at the appropriate sample azimuth angle [55]. The change in the polarization states before and after interaction with the metal tip is described by the tip-amplification tensor $\mathbf{A}$, Eq. (2), with an a-to-b ratio equal to $10:1$ (corresponding to a strongly polarization sensitive tip); the tip apex angle (see Section 2) was taken to be 50°.

The curves shown in Fig. 9(b) are the best fits to the experimental data; they were obtained for the following set of tensor component values, $\alpha_{xx} \sim 0.5$; $\alpha_{xz} \sim 0.3$, at two different sample azimuth angles. The somewhat lower fit quality on the right end side is to be ascribed to a signal fading resulting from the molecular photo-dissociation or photo-desorption under the action of the strongly enhanced local field (the so-called "bleaching effect"). It should be also noted that very similar curves were obtained considering the single-molecule tensor form $\mathbf{R}_{Ag}$ (Eq. (15)) implying that the actual near-field polarized scattering measurement does not make it possible to distinguish between the two possible molecular orientations within the unit cell. Possibly, the field enhancement extends over several contiguous domains rather than a single one and the retrieved values for the tensor components represent a local average.

Next, a careful inspection of Fig. 9 shows that, in contrast to the far-field curve peaking at 90° incident (p) polarization (within a 3° uncertainty in the orientation of the half-wave plate fast axis), the maximum intensities of the two near-field curves are slightly shifted from the 90° azimuth value (to lower azimuths, for the solid line and to higher azimuths, for the dashed one). These shifts are due to the non-zero off-diagonal components of the scattering tensor $\mathbf{R}_{azo}$ (and, more generally, $\mathbf{R}_{Ag}$); the magnitudes and signs of the shifts are also functions of the sample azimuth reflecting the local orientation of the domains with respect to the scattering plane. Recall that the two near-field curves were obtained for two different tip positions on the azobenzene layer surface and the two azimuth values used in the simulations reflect a different orientation of the domain(s) probed below the tip.

To reproduce the far-field behaviour (the solid curve in Fig. 9(a)), the same Raman tensor ($\mathbf{R}_{azo}$ from Eq. (16)) was used and the contributions produced by four equally spaced sample azimuth angles (0°; 90°, 180° and 270°) were summed up to account for the random orientation of the domains and the possible presence of disordered zones within the large illuminated area. Indeed, over a µm-scale laser spot, a great number of ordered domains are probed and their relative orientations remain spatially unresolved in the far-field response. As a result, the far-field polarization curve is peaking at 90°, in accordance with the random domain orientation in the *xy* plane.

In a conclusion, the validity of the near-field polarization model was experimentally tested on an ordered self-assembled non-crystalline (organic) structure. As a result, the Raman scattering tensor of the A_g-symmetry vibrations in the azobenzene molecule was quantitatively determined from the TERS measurements.

5. Conclusions and outlook

A certain number of conclusions, together with guidelines for future studies, can be drawn from the four case studies presented, originating from both far-field, as well as from near-field experiments.

The polarized far-field Raman spectroscopy in oblique backscattering configuration on semiconductor structures demonstrated its experimental capability to characterize strain in crystalline materials. Stress tensor determination with accuracy of several tens of MPa, signs included, could thus be achieved by varying the polarization state of the exciting laser radiation. Tensor component values for biaxial (bisotropic) stress states were obtained for SiGe plain, microelectronics structures. However, with the never-ending shrinking of the dimensions of the electronic devices, polarized near-field (TERS) experiments, rather than far-field ones, would be readily welcome for the characterization of local stresses at the nm scale (e.g., in field-effect transistor channels). An active research in this direction is currently under way.

By studying the variation of far-field Raman scattering response of pentacene thin films with the incident polarization, it became likewise possible to arrive at the correct group assignment of some "controversial" vibration modes leading to the unambiguous identification of two uncoupled (intramolecular) C–H bending vibrations. Besides revealing the power of the polarization-based approach to Raman scattering, this case study is clearly just a first, "far-field", step to a full Raman scattering tensor analysis performed in the near field.

The next step in this direction was the ν_{15}-vibration-mode Raman tensor determination of an azobenzene layer from TERS experiments. Having validated the near-field polarization model from Section 2 on a simple cubic crystal material (c-Si), we applied successfully the polarization approach to describe the response of the locally ordered self-assembled azobenzene monolayer, thus extending the validity of the model to non-crystalline organic materials.

From an instrumental viewpoint, a future development of the polarized Raman scattering equipment would necessarily include the implementation of a polarization state generator (PSG) and a polarization state analyzer (PSA), in lieu of the actually used half-wave plate and analyzer [56]. Through the generation and analysis of elliptical and not only linear polarization states, this upgrade will allow for the measurement of the complete polarimetric response (in the form of a Mueller–Stokes matrix) of the sample under investigation, thus going far beyond the polarized Raman approach described in the present work. The full polarimetric response would logically provide even more information than the polarized one thus making it possible to study the vibrational properties of complex materials and structures.

In summary, we have illustrated, on several experimental case studies, the usefulness of the implementation of polarization control in a Raman scattering experiment. The opportunities that open up are numerous and cover a variety of topics, of technological or of scientific interest, going from the stress analysis of semiconductor structures to Raman scattering tensor determination in TERS experiments on self-assembled organic monolayers.

Acknowledgements

The authors gratefully acknowledge financial support from Ile-de-France SESAME and ANR POLARAMAN and CONTRAM research contracts. One of the authors (G.N.) further recognizes a PhD sponsorship within a CIFRE contract with HORIBA Jobin Yvon. The authors are greatly indebted to C. Licitra from CEA-LETI, Grenoble for having provided them with the azobenzene solution, as well as to P. Morin from STMicroelectronics for the SiGe/Si strained structure sample.

References

[1] G. Turrell, J. Corset (Eds.), Raman Microscopy. Developments and Applications, Elsevier, Amsterdam, 1996.
[2] D.J. Gardiner, P.R. Graves (Eds.), Practical Raman Spectroscopy, Springer, Berlin, 1989.
[3] W.H. Weber, R. Merlin (Eds.), Raman Scattering in Materials Science, Springer, Berlin, 2000.
[4] I. De Wolf, H.E. Maes, S.K. Jones, J. Appl. Phys. 79 (1996) 7148.
[5] S. Narayanan, S.R. Kalidindi, L.S. Schadler, J. Appl. Phys. 82 (1997) 2595.
[6] I. De Wolf, J. Raman Spectrosc. 30 (1999) 877.
[7] B. Pettinger, B. Ren, G. Picardi, R. Schuster, G. Ertl, Phys. Rev. Lett. 92 (2004) 096101.
[8] M. Sackrow, C. Stanciu, M.A. Lieb, A.J. Meixner, Chem. Phys. Chem. 9 (2008) 316.
[9] A. Hartschuh, E.J. Sánchez, X.S. Xie, L. Novotny, Phys. Rev. Lett. 90 (2003) 095503.
[10] W. Zhang, B.S. Yeo, T. Schmid, R. Zenobi, J. Phys. Chem. C 111 (2007) 1733.
[11] G. Picardi, M. Chaigneau, R. Ossikovski, Chem. Phys. Lett. 469 (2009) 161.
[12] D.A. Long, The Raman effect. A Unified Treatment of the Theory of Raman Scattering by Molecules, Wiley, New York, 2002.
[13] R. Loudon, Adv. Phys. 13 (1964) 423.
[14] E. Anastassakis, J. Appl. Phys. 82 (1997) 1582.
[15] R. Ossikovski, Q. Nguyen, G. Picardi, Phys. Rev. B 75 (2007) 045412.
[16] A.L. Demming, F. Festy, D. Richards, J. Chem. Phys. 122 (2005) 184716.
[17] L. Aigouy, A. Lahrech, S. Grésillon, H. Cory, A.C. Boccara, J.C. Rivoal, Opt. Lett. 24 (1999) 187.
[18] G. Picardi, Q. Nguyen, J. Schreiber, R. Ossikovski, Eur. Phys. J. Appl. Phys. 40 (2007) 197.
[19] B. Ren, G. Picardi, B. Pettinger, Rev. Sci. Instrum. 75 (2004) 837.
[20] J. Michl, E.W. Thulstrup, Spectroscopy with Polarized Light, VCH, Weinheim, 1986.
[21] L. Barron, Molecular Light Scattering and Optical Activity, Cambridge University Press, Cambridge, 2004.
[22] M.L. Lee, E.A. Fitzgerald, M.T. Bulsara, M.T. Currie, A. Lochtefeld, J. Appl. Phys. 97 (2005) 011101.
[23] E. Anastassakis, in: D.J. Lockwood, J.F. Young (Eds.), Light Scattering in Semiconductor Structures and Superlattices, Plenum Press, New York, 1991.
[24] E. Bonera, M. Fanciulli, D.N. Batchelder, J. Appl. Phys. 94 (2003) 2729.

[25] G.H. Loechelt, N.G. Cave, J. Menéndez, J. Appl. Phys. 86 (1999) 6164.
[26] R. Ossikovski, Q. Nguyen, G. Picardi, J. Schreiber, P. Morin, J. Raman Spectrosc. 39 (2008) 661.
[27] M. Becker, H. Scheel, S. Christiansen, H.P. Strunk, J. Appl. Phys. 101 (2007) 063531.
[28] R. Ossikovski, Q. Nguyen, G. Picardi, J. Schreiber, J. Appl. Phys. 103 (2008) 093525.
[29] J.C. Tsang, P.M. Mooney, F. Dacol, J.O. Chu, J. Appl. Phys. 75 (1994) 8098.
[30] J. Cornil, J.-L. Brédas, J. Zaumseil, H. Sirringhaus, Adv. Mater. (Weinheim) 19 (2007) 1791.
[31] I. Stenger, A. Frigout, D. Tondelier, B. Geffroy, R. Ossikovski, Y. Bonnassieux, Appl. Phys. Lett. 94 (2009) 133301.
[32] T. Jentzsch, H.J. Juepner, K.-W. Brzezinka, A. Lau, Thin Solid Films 315 (1998) 273.
[33] M. Cazayous, A. Sacuto, G. Horowitz, Ph. Lang, A. Zimmers, R.P.S. Lobo, Phys. Rev. B 70 (2004) 081309.
[34] H.L. Cheng, Y.S. Mai, W.Y. Chou, L.R. Chang, Appl. Phys. Lett. 90 (2007) 171926.
[35] R. He, I. Dujovne, L. Chen, Q. Miao, C.F. Hirjibehedin, A. Pinczuk, C. Nuckolls, C. Kloc, A. Ron, Appl. Phys. Lett. 84 (2004) 987.
[36] P. Potera, I. Stefaniuk, M. Kuźma, Centr. Eur. J. Phys. 5 (2007) 165.
[37] E.V. Tsiper, Z.G. Soos, Phys. Rev. B 68 (2003) 085301.
[38] M. Pedio, B. Doyle, N. Mahne, A. Giglia, F. Borgatti, S. Nannarone, S.K.M. Henze, R. Temirov, F.S. Tautz, L. Casalis, R. Hudej, M.F. Danisman, B. Nickel, Appl. Surf. Sci. 254 (2007) 103.
[39] T. Ichimura, H. Watanabe, Y. Morita, P. Verma, S. Kawata, Y. Inouye, J. Phys. Chem. C 111 (2007) 9460.
[40] N. Anderson, A. Hartschuh, S. Cronin, L. Novotny, J. Am. Chem. Soc. 127 (2005) 2533.
[41] M. Chaigneau, G. Picardi, R. Ossikovski, Surf. Sci. 604 (2010) 701.
[42] G. Picardi, Q. Nguyen, R. Ossikovski, J. Schreiber, Appl. Spectrosc. 61 (2007) 1301.
[43] Q. Nguyen, R. Ossikovski, J. Schreiber, Opt. Commun. 74 (2007) 231.
[44] A. Merlen, J.-C. Valmalette, P. Gucciardi, M. Lamy de la Chapelle, A. Frigout, R. Ossikovski, J. Raman Spectrosc. 40 (2009) 1361.
[45] G. Picardi, M. Chaigneau, R. Ossikovski, C. Licitra, J. Raman Spectrosc. 40 (2009) 1407.
[46] A. Ulman, Chem. Rev. 96 (1996) 1533.
[47] H. Wolf, H. Ringsdorf, E. Delamarche, T. Takami, H. Kang, B. Michel, Ch. Gerber, M. Jaschke, H.J. Butt, E. Bamberg, J. Phys. Chem. 99 (1995) 7102.
[48] D.R. Armstrong, J. Clarkson, W.E. Smith, J. Phys. Chem. 99 (1995) 17825.
[49] V. Stepanic, G. Baranovic, V. Smrecki, J. Mol. Struct. 569 (2001) 89.
[50] S.W. Han, C.H. Kim, S.H. Hong, Y.K. Chung, K. Kim, Langmuir 15 (1999) 1579.
[51] K. Tamada, J. Nagasawa, F. Nakanishi, K. Abe, T. Ishida, M. Hara, W. Knoll, Langmuir 14 (1998) 3264.
[52] T.G. Pedersen, P.S. Ramanujam, P.M. Hvilsted, J. Opt. Soc. Am. B 15 (1998) 2721.
[53] R. Wang, T. Iyoda, L. Jiang, K. Hashimoto, A. Fujishima, Chem. Lett. 25 (1996) 1005.
[54] S.C.B. Mannsfeld, T.W. Canzler, T. Fritz, H. Proehl, K. Leo, S. Stumpf, G. Goretzki, K. Gloe, J. Phys. B 106 (2002) 2255.
[55] M. Chaigneau, G. Picardi, R. Ossikovski, Int. J. Mol. Sci. 12 (2011) 1245.
[56] A. Frigout, M. Richert, R. Ossikovski, Eur. Phys. J. Web Conf. 5 (2010) 06002.